Thermodynamic properties of the Nd-Bi system via emf measurements, DFT calculations, machine learning, and CALPHAD modeling

Sanghyeok Im, Shun-Li Shang, Nathan D. Smith, Adam M. Krajewski, Timothy Lichtenstein, Hui Sun, Brandon J. Bocklund, Zi-Kui Liu, Hojong Kim*

Department of Materials Science and Engineering, The Pennsylvania State University, University Park, PA 16802, United States

Author e-mail addresses:

svi5106@psu.edu, sus26@psu.edu, nds174@psu.edu, ak@psu.edu, tvl5297@psu.edu, suh960@psu.edu, bocklund@psu.edu, zxl15@psu.edu, huk29@psu.edu

Corresponding author:

*E-mail: huk29@psu.edu. Tel: 814-865-3117. Fax: 814-865-2917

ABSTRACT

Thermodynamic properties of the Nd-Bi system were investigated using a combination of experimental measurements, first-principles calculations based on density functional theory (DFT), data mining and machine learning (DM + ML) predictions, and calculation of phase diagrams (CALPHAD) modeling. The electromotive force (emf) of Nd-Bi alloys in molten LiCl-KCl-$NdCl_3$ at 773–973 K was measured via coulometric titration of Nd in Bi for the determination of thermochemical properties such as activity coefficients and solubilities of Nd in Bi. A new peritectic reaction of [liquid + $NdBi_2$ = Nd_3Bi_7] at 774 K was confirmed using differential scanning calorimetry, structural (X-ray diffraction), and microstructural (scanning electron microscopy) analyses. The unknown crystal structure of $NdBi_2$ was suggested to be a mixture of the anti-La_2Sb configuration and the La_2Te-type configuration based on ML predictions for over 26,000 data-mined AB_2-type configurations together with DFT-based verifications. Using the newly acquired experimental data and DFT-based calculations, the thermodynamic description of the Nd-Bi system was remodeled, and a more complete Nd-Bi phase diagram was calculated, including the Nd_3Bi_7 compound, invariant transition reactions, and liquidus temperatures.

KEYWORDS:

Rare-earth alloys, Nd-Bi phase diagram, emf measurement, first-principles calculations, machine learning, CALPHAD modeling

1 Introduction

Thermodynamic properties of rare-earth elements are essential in the rational design of rare-earth alloys for clean energy technologies (e.g., permanent magnet motors for electric vehicles and wind turbines) as well as the development of efficient rare-earth recovery processes for a sustainable materials cycle [1–3]. Liquid metals (e.g., Bi and Sn) have been investigated as an electrode material for electrochemical recovery of reactive elements (alkali/alkaline-earth, rare-earth metals) and for energy storage devices (liquid metal batteries), utilizing strong chemical interactions for enhanced recovery efficiency or high cell voltage [4,5]. The electrochemical recovery of rare-earth elements (e.g., Nd) using liquid metals would require reliable thermodynamic knowledge including activity, solubility, and phase transitions of rare-earth metals and alloys. Therefore, the present work investigated thermodynamic properties of the binary Nd-Bi system by integrating experimental measurements (electrochemical, thermal, and structural analyses) with advanced computational modeling such as high-throughput machine learning (ML) predictions of crystal structures, first-principles calculations based on density functional theory (DFT), and the CALPHAD (CALculation of PHAse Diagram) approach.

Thermodynamic properties of Nd-Bi alloys were assessed by Wang et al. [6] based on experimental results, including differential thermal analysis (DTA) by Abulkhaev [7], direct calorimetry by Borsese et al. [8], and the Knudsen effusion method for NdBi by Viksman and Gordienko [9]. The calculated Nd-Bi phase diagram included five intermetallic compounds: $NdBi_2$, NdBi, Nd_4Bi_3, Nd_5Bi_3, and Nd_2Bi. Recently, new experimental information was reported, including a new intermetallic compound (Nd_3Bi_7) by Ovchinnikov et al.[10], emf data for dilute Nd compositions (mole fraction, $x_{Nd} < 0.0025$ at 773–873 K) by Yin et al. [11] and for the two-phase Nd-Bi alloys ($x_{Nd} = 0.15$–0.40 at 725–1075 K) by Lichtenstein et al. [12], and solubility of

Nb in Bi (*cf.*, Sec. 3). Of these previous results, some solubility and activity data of Nd for Bi-rich alloys are inconsistent, leading to uncertainty in estimating the capacity of liquid Bi for Nd recovery. For example, the solubility of Nd in liquid Bi was reported at 9.55 mol% at 973 K by Abulkhaev [7] via DTA analysis, but was reported at 4.64 mol% by Smith [13] via chemical analysis of Nd-saturated liquid alloys. In order to develop a more complete thermodynamic understanding of the Nd-Bi system, the inconsistent and incomplete properties will be a focus of experimental measurements in the present work.

The present work measured the emf values of the Nd-Bi alloys both in single-phase (liquid) and two-phase compositions up to $x_{Nd} = 0.07$ via coulometric titration of Nd into liquid Bi in molten LiCl-KCl-$NdCl_3$ electrolyte at 773–973 K. The emf data were used to determine the solubilities, activity coefficients, and phase transitions of the Nd-Bi alloys. Phase transitions in the Nd-Bi alloys ($x_{Nd} = 0.06–0.40$) were further elaborated using differential scanning calorimetry (DSC) to characterize transition reactions associated with the Nd_3Bi_7 compound, in complement with structural and microstructural characterization via X-ray diffraction (XRD) and scanning electron microscopy (SEM).

Thermodynamic properties of the Nd-Bi compounds were calculated by DFT-based calculations to provide initial inputs for CALPHAD modeling, validate thermodynamic stability of each compound, and compare to available experimental data. It is noted that crystallographic information for $NdBi_2$ (e.g., atomic positions) was unknown [14] and was thus examined computationally in the present work by (i) a data-mining approach in terms of a structure-informed ML prediction of enthalpy of formation [15] for over 26,000 AB_2-type configurations reported in the literature followed by DFT-based verifications for the low-energy configurations, and (ii) a Universal Structure Predictor: Evolutionary Xtallography (USPEX) [16,17] with DFT-based calculations as a computational engine. Lastly, the present work remodeled thermodynamic properties of the Nd-Bi binary system by incorporating new experimental (activities, solubilities, and phase transitions) and computational data, building upon the previous thermodynamic modeling by Wang et al. [6].

2 Methodology

2.1 Electrochemical cell for emf measurements of the Nd-Bi alloys

The electrochemical cell for Nd-Bi emf measurements can be written as:

$$(-)\ \underline{\mathrm{Nd(s)}}\ |\ \text{electrolyte}\ |\ \mathrm{Nd(in\ Bi)}\ (+) \qquad \text{Eq. 1}$$

where Nd(s) serves as the reference electrode (RE) and the Nd-Bi alloys are working electrodes (WE) in an electrolyte where Nd^{3+} ions are the most electroactive component. The half reactions for this electrochemical cell are:

$$\text{WE } (+)\text{: } \mathrm{Nd^{3+}} + 3\mathrm{e^-} = \mathrm{Nd(in\ Bi)} \qquad \text{Eq. 2}$$

$$\text{RE } (-)\text{: } \mathrm{Nd^{3+}} + 3\mathrm{e^-} = \mathrm{Nd(s)} \qquad \text{Eq. 3}$$

and the overall cell reaction is:

$$\text{Overall: } \mathrm{Nd(s)} = \mathrm{Nd(in\ Bi)}. \qquad \text{Eq. 4}$$

The change in partial molar Gibbs energy of Nd, $\Delta\bar{G}_{\mathrm{Nd}}$, for this cell reaction is given by:

$$\Delta\bar{G}_{\mathrm{Nd}} = \bar{G}_{\mathrm{Nd(in\ Bi)}} - G^{0}_{\mathrm{Nd}} = RT\ln(a_{\mathrm{Nd}}), \qquad \text{Eq. 5}$$

where R is the universal gas constant, T the absolute temperature, $\bar{G}_{\mathrm{Nd(in\ Bi)}}$ the partial molar Gibbs energy (chemical potential), and a_{Nd} the activity of Nd in Bi. The cell emf of a Nd-Bi alloy (E_{eq}) is related to $\Delta\bar{G}_{\mathrm{Nd}}$ and the activity by the Nernst equation:

$$E_{\mathrm{eq}} = -\frac{\Delta\bar{G}_{\mathrm{Nd}}}{3F} = -\frac{RT}{3F}\ln(a_{\mathrm{Nd}}) \qquad \text{Eq. 6}$$

where F is the Faraday constant.

It is well known that pure Nd reacts readily with molten chlorides by disproportionation reaction ($Nd + 2NdCl_3 \rightarrow 3NdCl_2$) and thus, is not suitable for reliable emf measurements in molten chlorides [12,18,19]. However, our recent work [12] demonstrated that a Nd-Sn alloy (x_{Nd} = 0.10) can be employed as a stable RE in LiCl-KCl-$NdCl_3$ at 725–1100 K, utilizing its two-phase [L (liquid) + $NdSn_3$] behavior and reduced reactivity compared to pure Nd(s). Therefore, the present work employed a less reactive Nd-Sn alloy (x_{Nd} = 0.10) as the new RE and the cell potential of the Nd-Bi alloys (E_{I}) were measured using:

$$\text{I: } \underline{\text{Nd(in Sn)}^*} \mid \text{LiCl-KCl-NdCl}_3 \mid \text{Nd(in Bi)}, \qquad E_{\mathrm{I}} = -\frac{RT}{3F}\ln\left(\frac{a_{\mathrm{Nd}}}{a^*_{\mathrm{Nd}}}\right) \qquad \text{Eq. 7}$$

where a^*_{Nd} is the activity of Nd in Sn at x_{Nd} = 0.10. The cell potential (E_{II}) of the two-phase Nd-Sn alloy at x_{Nd} = 0.10 relative to pure Nd(s) was previously established and exhibited linear behavior at 724–1075 K [12]:

$$E_{\mathrm{II}} = -\frac{RT}{3F}\ln(a^*_{\mathrm{Nd}}) = 0.590 + 1.52 \times 10^{-4}\, T \text{ [V] vs. Nd(s).} \qquad \text{Eq. 8}$$

In the present work, the cell emf (E_{eq}) of a Nd-Bi alloy relative to pure Nd(s) was obtained by adding the two cell potentials ($E_{\mathrm{eq}} = E_{\mathrm{I}} + E_{\mathrm{II}}$) at a given temperature.

2.2 Electrochemical measurements of the Nd-Bi alloys

2.2.1 Fabrication of electrochemical cell components

The ternary LiCl-KCl-$NdCl_3$ electrolyte (eutectic LiCl-KCl + 2 mol% $NdCl_3$) was prepared from appropriate weights of LiCl (Ultra dry, 99.9%, Alfa Aesar), KCl (Ultra dry, 99.95%, Alfa Aesar), and $NdCl_3$ (anhydrous, 99.5%, Alfa Aesar) powders. The powder mixture was loaded into a quartz crucible (Technical Glass Products) for pre-melting in a stainless-steel vacuum chamber. The chamber was loaded in a crucible furnace (Mellen, CC-12), evacuated to ~1 Pa, and heated under vacuum at 373 K for 12 h and at 543 K for 12 h to dry the salt mixture. The chamber was then purged with ultra-high purity argon gas and heated to 973 K for 3 h under a slowly flowing (50 mL min^{-1}) argon atmosphere. After cooling, the dry and homogeneous electrolyte was ground into fine powder using a mortar and pestle for use in the electrochemical cell.

The pure Bi WE was fabricated by induction melting 2.02 g of pure Bi in a boron nitride (BN) crucible (20 mm height, 12 mm OD, 8 mm ID, and 17 mm depth) using an induction heater (IH15A-2T, Across International) custom-installed inside an Ar-filled glovebox (O_2 < 0.5 ppm). The nominal surface area of the WE was estimated to be 0.5 cm^2. The Nd-Sn alloy (x_{Nd} = 0.10) was fabricated using a laboratory arc-melter (MAM-1, Edmund Bühler GmbH) under an inert argon atmosphere from pure Nd (99.1%, Alfa Aesar) and Sn (99.9999%, Alfa Aesar) metals. The Nd-Sn alloy RE was re-melted inside a BN crucible (35 mm height, 12 mm OD, 8 mm ID, and 30 mm depth) via induction heating. Two 1 mm diameter capillary holes were drilled 7 mm above the bottom of the BN crucible to establish contact with the electrolyte. The liquid Nd-Bi (x_{Nd} = 0.03) counter electrode (CE) was fabricated by adding Nd pieces in a liquid Bi (99.999%, Sigma-Aldrich) in a BN crucible (15 mm height, 25 mm OD, 22 mm ID, and 11 mm depth) using the induction heater. Electrical contact for each electrode was established by immersing an inert tungsten wire (1 mm diameter) in liquid Bi during induction heating. The three-electrode cell configuration is shown in **Figure 1**.

[Figure 1]

2.2.2 Electrochemical cell assembly and measurements

The final assembly of the electrochemical cell was conducted in an Ar-filled glovebox. The electrodes were placed in an alumina crucible (AdValue Technology) and the electrolyte powder was poured over the electrodes; the tungsten electrical leads were insulated from the test chamber using an alumina tube and sealed at the top with epoxy. The three-electrode cell assembly was then loaded into a stainless-steel test chamber, sealed in the glovebox, loaded into a crucible furnace, and evacuated to ~1 Pa. The electrochemical cell was vacuum-dried using the same procedure for preparing the electrolyte and heated to 773 K under flowing argon. The cell temperature was measured using a thermocouple (ASTM, Type-K) located in the electrolyte and data acquisition system (NI 9211, National Instruments).

The electrochemical measurements were conducted using a potentiostat-galvanostat (Autolab PGSTAT302N) at 773–973 K. The composition of Nd in the Bi WE was continually changed by depositing Nd under a constant cathodic current density of 25 mA cm^{-2} for 550 s in each coulometric titration step, followed by open-circuit potential (OCP) measurement for 1–2 h to allow for homogenization of the Nd-Bi alloy.

2.3 Characterization of the Nd-Bi alloys

Differential scanning calorimetry (DSC) was performed at 473−1023 K to determine phase transitions of the Nd-Bi alloys (x_{Nd} = 0.06–0.40) using a thermal analyzer (Netzsch, STA 449 F3 Jupiter). Approximately 20−50 mg of arc-melted samples were placed on tungsten foil inside the alumina crucible to prevent side reactions between the alloy and the crucible. The DSC data were collected during heating/cooling cycles at multiple scan rates of 5−20 K min^{-1} under flowing Ar (20 mL min^{-1}).

Phase identification of the Nd-Bi alloys was conducted using X-ray diffractometry (XRD, PANalytical Empyrean, Cu Kα-radiation) over 2θ angles of 20−70°. The Nd-Bi alloys for XRD measurements were annealed for 96 h at 753 K for x_{Nd} = 0.20 and 0.31 or at 913 K for x_{Nd} = 0.40. The annealed samples were ground into fine powders in the Ar-filled glovebox and coated with mineral oil to minimize oxidation during the XRD measurements. Three Nd-Bi alloys were annealed for 6 days at 753 K for $x_{Nd} = 0.20$ and 0.31 or at 913 K for $x_{Nd} = 0.40$ to characterize their microstructures using a scanning electron microscope (SEM, FEI Quanta 200) fitted with energy-dispersive spectroscopy (EDS). The annealed Nd-Bi alloys were mounted in epoxy resin, then the surface was polished up to 2000 grit using silicon carbide abrasive paper and isopropyl alcohol.

2.4 Calculation of thermodynamic properties of Nd-Bi compounds

2.4.1 Crystallographic configuration of $NdBi_2$ from ML and USPEX

The possible configurations of $NdBi_2$ were determined by a novel data-mining approach in terms of ML predictions of enthalpy of formation (ΔH_0) together with DFT-based verifications. As shown in **Figure S1**, all of the AB_2-type configurations (26,055) were first identified within a large dataset of DFT-relaxed or experimental structures (~1.3 million at the time of extraction) contained within the recently developed Material-Property-Descriptor Database (MPDD) [20] oriented towards efficient machine learning at large scales. This MPDD query covered all materials contained in the Open Quantum Materials Database (OQMD) [21], the Materials Project (MP) database [22], the Joint Automated Repository for Various Integrated Simulations (JARVIS) database [23], and the Crystallography Open Database (COD) [24,25]. As a result, 26,055 AB_2-type configurations were selected and their compositions were substituted with $NdBi_2$, creating the same number of candidates for a stable $NdBi_2$ structure. Following the substitution, all of the candidates were examined by a recently developed ML tool called SIPFENN (Structure-Informed Prediction of Formation Energy Using Neural Networks) [15] (see **Figure S1**) to identify configurations with the lowest formation enthalpy. SIPFENN is a model designed to be very general and require only structure files (such as POSCAR or CIF) as inputs, allowing straightforward integration into this data-mining study. On a random 5% subset in the OQMD structures, SIPFENN could achieve a test set mean absolute error (MAE) of 28 meV/atom (2.7 kJ/mol-atom) to predict ΔH_0 [15].

More than five hundred AB_2-type configurations were selected with low ΔH_0 values up to 12 kJ/mol-atom variation and subjected to initial DFT-based verifications. For 20 configurations with the lowest ΔH_0 values from the initial DFT-based verifications, more detailed DFT calculations were performed to obtain the energy versus volume equation of states described in the following section. Note that the selected configurations, while all AB_2-type, possess different space groups and/or different Wyckoff positions (see the Supplementary Excel file).

In addition to the data-mining approach with ML predictions and DFT-based verifications, the possible $NdBi_2$ configurations were also examined using the universal structure predictor—USPEX [16,17] in terms of a 24-atom unit cell where the computational engine of USPEX is the DFT-based calculations as detailed in Sec. 2.4.2. USPEX is an evolutionary algorithm that searches for the lowest energy configuration/structure using only supercell size and atomic species as inputs. USPEX simulations are self-improving, i.e., in the subsequent generations the good structures are found and used to generate new structures. The efficiency of USPEX draws from carefully designed variation operators, while its reliability is largely due to the use of state-of-the-art first-principles simulations inside the evolutionary algorithm [16,17], which has been demonstrated for a range of different materials such as the unexpected stable stoichiometries of sodium chlorides [26] and the post-perovskite phase of $MgSiO_3$[27].

2.4.2 DFT-based first-principles calculations

All DFT-based first-principles calculations in the present work were performed by the Vienna *Ab initio* Simulation Package (VASP) [28] with the ion-electron interaction described by the projector augmented wave method [29]. The adopted exchange-correlation (X-C) functionals were the generalized gradient approximation (GGA) developed by Perdew, Burke, and Ernzerhof (PBE) [30]. In addition, the GGA improved for densely packed solids and their surfaces (i.e., the PBEsol or the PS potential) [31] and the meta-GGA of the strongly constrained and appropriately normed (SCAN) functional [32] were also employed. The selected electronic configurations include 11 valences for Nd (e.g., the Nd_3 as labeled by VASP) and 15 for Bi (e.g., the Bi_d). Structural details of the Nd-Bi compounds are referred to the entries either in Materials Project [22] or in OQMD [21] when possible (see the Supplementary Excel file). The exceptions are for the compound of Nd_3Bi_7 [10] and the configuration of $NdBi_2$ predicted by USPEX with 24 atoms in the unit cell (labeled as USPEX24), see **Table S1**. In VASP calculations, a final cutoff energy of 520 eV was used for the plane-wave basis set, and the *k*-point meshes are given in the Supplementary Excel file. The energy convergence criterion of electronic self-consistency was at least 10^{-6} eV per atom for the final calculations. The reciprocal-space energy integration for relaxations was performed by the Methfessel-Paxton [33] technique, while the final calculations were performed by the tetrahedron method incorporating a Blöchl correction [34]. Regarding VASP calculations related to the universal structure predictor, the settings suggested from the USPEX were employed for $NdBi_2$, where the initial supercell with 24 atoms (16 Bi and 8 Nd) was selected and created by USPEX.

For each Nd-Bi compound, its energy versus volume (E-V) data points were predicted by DFT-based first-principles calculations. These E-V data points were fitted by a four-parameter Birch-Murnaghan equation of state (EOS) [35]:

$$E(V) = k_1 + k_2 V^{-2/3} + k_3 V^{-4/3} + k_4 V^{-2} \qquad \text{Eq. 9}$$

where k_1, k_2, k_3, and k_4 are fitting parameters. Equilibrium properties at zero external pressure (P = 0 GPa) from this E-V EOS include energy E_0 (i.e., the enthalpy H_0 at P = 0 GPa), volume V_0, bulk modulus B_0, and the pressure derivative of bulk modulus B'. Eight data points were typically employed to estimate equilibrium properties for each EOS fitting. In addition, E-V EOS fitting error can be estimated by $\sqrt{\sum\left[(E_{fit} - E_{calc})/E_{calc}\right]^2/n}$, where E_{fit} and E_{calc} are the fitted and the first-principles calculated energies, respectively, and n represents the total number of calculated points [35].

2.5 CALPHAD modeling of the Nd-Bi system

2.5.1 Thermodynamic models

The thermodynamic models in this work are the same as those in the previous CALPHAD modeling of the Nd-Bi system by Wang et al. [6]. For solution phases, ϕ, such as liquid, body centered cubic (BCC), double hexagonal close-packed (DHCP), and rhombohedral A7 (Rho_A7), molar Gibbs energy is expressed as follows:

$$G_{\mathrm{m}}^{\phi} = \sum_{i=\mathrm{Bi,Nd}} x_i\, {}^0G_i^{\phi} + RT \sum_{i=\mathrm{Bi,Nd}} x_i \ln x_i + x_{\mathrm{Bi}} x_{\mathrm{Nd}} \sum_{j=0}^{n} {}^jL^{\Phi}\, (x_{\mathrm{Bi}} - x_{\mathrm{Nd}})^j \qquad \text{Eq. 10}$$

where x_i is the mole fraction of element i (Bi or Nd), ${}^0G_i^{\Phi}$ is the Gibbs energy of pure element i (Bi or Nd) with respect to their standard element reference (SER) states at P = 1 bar and T = 298.15 K, taken from the Scientific Group Thermodata Europe (SGTE) pure elements database compiled by Dinsdale [36], and ${}^jL^{\Phi}$ is the jth interaction parameter of phase ϕ:

$${}^jL^{\phi} = a^{\phi} + b^{\phi}T \qquad \text{Eq. 11}$$

where a^{ϕ} and b^{ϕ} are modeling parameters.

For each stoichiometric compound of Nd_pBi_q, including Nd_3Bi_7 (space group $Immm$, #71)[10], $NdBi_2$ (the distorted anti-La_2Sb structure) [14], NdBi ($Fm\overline{3}m$, #225) [14], Nd_4Bi_3 ($I\overline{4}3d$, #220) [14], Nd_5Bi_3 ($P6_3mcm$, #193) [14], and Nd_2Bi ($I4/mmm$, #139) [14], molar Gibbs energy is expressed as follows with the (p + q) normalized to the sum of one (**Table 2**):

$$G_{\mathrm{m}}^{\mathrm{Nd_pBi_q}} = \mathrm{p}\ {}^{0}G_{\mathrm{Nd}}^{\mathrm{DHCP}} + \mathrm{q}\ {}^{0}G_{\mathrm{Bi}}^{\mathrm{Rho\_A7}} + a^{\mathrm{Nd_pBi_q}} + b^{\mathrm{Nd_pBi_q}}T \qquad \text{Eq. 12}$$

where $a^{\mathrm{Nd_pBi_q}}$ and $b^{\mathrm{Nd_pBi_q}}$ are modeling parameters as those shown in Eq. 11. ${}^{0}G_{\mathrm{Bi}}^{\mathrm{Rho\_A7}}$ and ${}^{0}G_{\mathrm{Nd}}^{\mathrm{DHCP}}$ are the Gibbs energies of Bi and Nd, respectively, taken from the SGTE database [36].

2.5.2 CALPHAD modeling by ESPEI/PyCalphad

By considering the new phase of Nd_3Bi_7 identified by Ovchinnikov et al. [10]and the present emf measurements of activity, liquidus, and decomposition temperature of Nd_3Bi_7 (**Table 1**, **Table S2**, and **Table S3**), the Nd-Bi system was re-modeled in the present work using the open source software ESPEI (Extensible Self-optimizing Phase Equilibrium Infrastructure) [37] with the computational engine of PyCalphad [38]. PyCalphad is a Python library for designing thermodynamic models, calculating phase diagrams, and investigating phase equilibria using the CALPHAD method [39,40]. ESPEI uses thermochemical data and phase diagram data represented in JSON (JavaScript Object Notation) files to perform a CALPHAD assessment through a two-step procedure of parameter generation and Bayesian parameter estimation. Parameter generation rapidly fits the Gibbs energies of endmembers and interaction parameters from thermochemical data. The Bayesian parameter estimation uses Markov Chain Monte Carlo (MCMC) sampling method to optimize and quantify the uncertainty of all model parameters simultaneously using thermochemical data with fixed internal degrees of freedom, equilibrium thermochemical data, and phase boundary data. During the MCMC simulations, proposed sets of parameters will be accepted or rejected based on the Metropolis criteria [37], that enables the uncertainty quantification (UQ) of the parameters [41]. Samples from the Markov chains of accepted parameters are propagated to estimate uncertainties for any thermodynamic properties of interest. For example, for the activity in liquid, each sample has its own activity value corresponding to the parameters generated in each MCMC iteration. The uncertainty of activity represents the range of the possible activity values from a set of samples. In the present work, four chains were employed for each modeling parameter. The initial parameters values for each chain were generated by sampling from an uncorrelated Gaussian distribution [37] centered on $\boldsymbol{p}$ with a standard deviation $0.01\boldsymbol{p}$, where $\boldsymbol{p}$ is the vector of parameters from the starting point generation. At least 200 MCMC steps were performed for the ESPEI/PyCalphad modeling, and the chain values in the last MCMC step were employed to estimate the UQ values.

3 Results and discussion

3.1 Emf measurements of Nd-Bi alloys via coulometric titration

The emf measurements of the Nd-Bi alloys were conducted via a coulometric titration technique where Nd is deposited into the Bi WE with a constant current and then the Nd-Bi alloy electrode is held under open circuit conditions to reach a homogeneous composition and steady OCP at 773–973 K (**Figure 2**a). As the Nd composition increases, the OCP of the Nd-Bi alloy shifts in the negative direction in liquid state and reaches a constant value due to a phase transition into a two-phase [liquid + solid] region. The transition into a two-phase region was also evident during the Nd deposition (**Figure 2**b), indicated by a steep potential drop associated with the nucleation of a Nd-Bi intermetallic compound (nucleation overpotential) at 773 K and 873 K. The formation of the Nd-Bi intermetallic compounds (Nd_3Bi_7, $NdBi_2$, and NdBi) depends on the temperature and will be discussed in the following section based on the characterization of the Nd-Bi alloys.

[Figure 2]

At each titration step, the mole fraction of the Nd was calculated using Faraday's law and the emf was obtained from the average of steady OCP for the last 0.5 h of each step. The measured emf values (E_{I}) were converted to the emf (E_{eq}) versus pure Nd using Eq.8 [12]. The emf (E_{eq}) of the Nd-Bi alloy is plotted in **Figure 3**a as a function of x_{Nd} at 773−973 K. As Nd composition increases, the emf values decrease in the liquid phase and then remain constant in the two-phase region where the activity of Nd is constant with respect to the composition in the binary system based on the Gibbs phase rule.

[Figure 3]

At dilute compositions ($x_{\mathrm{Nd}} < 0.0025$), the emf values in this work are comparable to the results by Yin et al. at 873 K [11]. The emf values of the Nd-Bi alloys relative to pure Nd(s) were used to calculate the activity of Nd (Eq. 6) as well as the partial molar excess Gibbs energy ($\Delta\bar{\mathrm{G}}_{\mathrm{Nd}}^{\mathrm{ex}}$):

$$\Delta\bar{G}_{\mathrm{Nd}}^{\mathrm{ex}} = RT(\ln a_{\mathrm{Nd}} - \ln x_{\mathrm{Nd}}) = RT\ln\gamma_{\mathrm{Nd}} \qquad \text{Eq. 13}$$

where γ_{Nd} is the activity coefficient, summarized in **Table S2**. The activity coefficient of Nd in liquid alloy remains constant (Henrian behavior) and is as low as $\gamma_{\mathrm{Nd}}{\sim}10^{-12}$ (**Figure 3**b), indicating a strong chemical interaction and non-ideal solution behavior of the Nd-Bi alloys. Compared to the previous works at 873 K [11,13], this work was in excellent agreement with the result from Yin et al. ($\gamma_{\mathrm{Nd}}{\sim}10^{-11}$), but was substantially different from the result ($\gamma_{\mathrm{Nd}}{\sim}10^{-8}$) estimated by Smith [13].

In addition, the solubility of Nd in liquid Bi was determined from the intersection of the distinct emf trajectories for the two-phase region and the liquid single-phase region at each temperature (vertical line in **Figure 3**a), summarized in **Table 1**. The solubility of Nd in liquid Bi was as low as 0.99 mol% at 773 K and increased up to 5.65 mol% at 973 K, illustrating the utility of the coulometric titration in determining the emf of Nd-Bi alloys as well as delineating the solubility of Nd. The solubility values of Nd in liquid Bi were in close agreement with those measured by Smith [13] within 1 mol% difference, but were much lower than those from Abulkhaev [7] by about 4 mol%. This large discrepancy with Abulkhaev's work [7] is thought to originate from the insensitivity of the thermal analysis in determining the liquidus temperatures for dilute Nd compositions.

[**Table 1**]

3.2 Characterization of Nd-Bi alloys

3.2.1 Phase transition temperatures by DSC

The phase transition temperatures of the Nd-Bi alloys ($x_{\mathrm{Nd}} = 0.06–0.40$) were determined via DSC measurements between 472–1023 K at scan rates of 5–20 K min^{-1}. Representative DSC data are shown in **Figure 4** for the 20 K min^{-1} scan rate. Three characteristic transition reactions (I–III), were observed: eutectic reaction [I: L = Bi + Nd_3Bi_7] at 539 K, peritectic reaction [II: L + $NdBi_2$ = Nd_3Bi_7] at 774 K, and peritectic reaction [III: L + NdBi = $NdBi_2$] at 932 K (**Table S3**). It is noted that the peritectic reaction [II: L + $NdBi_2$ = Nd_3Bi_7] is a new addition to the Nd-Bi phase diagram based upon the characteristic transition temperature at 774 K and the recent identification of the Nd_3Bi_7 compound. Based upon the thermal analyses, the two-phase regions with constant emf (**Figure 3**a) are expected to be [L + Nd_3Bi_7] at 773 K, [L + $NdBi_2$] at 873 K, and [L + NdBi] at 973 K, respectively.

[**Figure 4**]

3.2.2 Analysis of phase constituents by SEM-EDS and XRD

The arc-melted Nd-Bi alloys were annealed for 6 days at 753 K for $x_{Nd} = 0.20$ and 0.31 or at 913 K for $x_{Nd} = 0.40$ for characterization by SEM-EDS (**Figure 5**). The composition of distinct phases in each alloy was averaged from EDS analysis at multiple points (> 10). For $x_{Nd} = 0.20$, the Bi phase and the Nd_3Bi_7 compound were observed (**Figure 5**a**)**. Multiple phases were evident for $x_{Nd} = 0.31$, including two metastable phases (Bi and NdBi) and a matrix composed of Nd_3Bi_7 and $NdBi_2$ based on the EDS analysis (**Figure 5**b). For $x_{Nd} = 0.40$, two distinct phases were identified with stoichiometry close to the $NdBi_2$ and NdBi intermetallic compounds (**Figure 5**c). The microstructural analyses of the annealed Nd-Bi alloys support the presence of Nd_3Bi_7 (at $x_{Nd} = 0.20$ and 0.31) and $NdBi_2$ (at $x_{Nd} = 0.31$ and 0.40) compounds, corroborating the characteristic phase transition reactions (I–III) from the DSC measurements.

[**Figure 5**]

The phase constituents of the annealed Nd-Bi alloys ($x_{Nd} = 0.20$, 0.31, and 0.40) were characterized by XRD and compared to the reported XRD patterns of Bi, Nd_3Bi_7, and NdBi with the exception of the $NdBi_2$ compound whose crystal structure and XRD pattern are not available in the literature (**Figure 6**) [10,14,42]. For $x_{Nd} = 0.20$, two equilibrium phases of Bi and Nd_3Bi_7 were clearly observed but the peak intensity from the Nd_3Bi_7 compound was much lower than that of the Bi phase (**Figure 6)**. Multiple phase constituents were detected comprising Bi, Nd_3Bi_7, and NdBi for $x_{Nd} = 0.31$, and NdBi was observed to be dominant at $x_{Nd} = 0.40$, in agreement with microstructural analyses by SEM-EDS. Considering the two-phase [$NdBi_2$ + NdBi] microstructure at $x_{Nd} = 0.40$, the additional peaks besides NdBi are thought to come from the $NdBi_2$ compound (**Figure 6**b). These additional peaks from $NdBi_2$ were also observed at $x_{Nd} = 0.31$; however, two peaks at $2\theta = 29.9°$ and 35.5° are included in the pattern of Nd_3Bi_7, complicating the phase analysis associated with $NdBi_2$ compound.

[**Figure 6**]

3.3 Calculated thermodynamic properties of Nd-Bi compounds

The thermodynamic properties of Nd-Bi compounds at $T = 0$ K were predicted by the X-C functional of SCAN and a fitting of the E-V EOS for each Nd-Bi compound or pure element, summarized in **Table S4** in comparison to experimental results. The complete set of predictions by the PBE, PS, and SCAN functionals are provided in the Supplementary Excel file. The V_0 values from SCAN agree with experimental data with the difference less than 0.6 Å^3/atom, except for $NdBi_2$. The volume $V_0 = 964$ Å^3 per unit cell for $NdBi_2$ was reported by Yoshihara et al. [14], but without mentioning the number of atoms in the unit cell. In comparison with the present DFT results of $NdBi_2$ in the Supplementary Excel file (around 30–32 Å^3/atom), the possible atoms should be 30 in the unit cell, resulting in the measured $V_0 = 32.13$ (964/30) Å^3/atom. Due to the unconfirmed number of atoms in the unit cell, we claim that the reported volume and lattice parameters of $NdBi_2$ [14] are less useful for comparison with the present DFT results. Regarding bulk modulus, the B_0 values of the Nd-Bi compounds are in the range of 52–59 GPa with the maximum value being for Nd_4Bi_3 and much higher than those of the pure elements Nd and Bi (< 37 GPa), while the B' values show a decreasing trend (from 5.9 to 2.7) with increasing x_{Nd} (**Table S4**).

The ΔH_0 values at $T = 0$ K for the 21 $NdBi_2$ configurations (No. 3 to No. 23) were predicted by first-principles calculations in terms of the X-C functionals of PBE, PS, and SCAN (**Figure 7**a) and the structural details of $NdBi_2$ are given in the Supplementary Excel file and **Table S1**. The variation of the ΔH_0 values predicted by each X-C functional is about 10 kJ/mol-atom starting from the lowest ΔH_0 of configuration No. 3 (i.e., the USPEX24). The SCAN functional predicts the lowest ΔH_0, followed by the predictions by PS and then by PBE. In general, the low energy configurations of $NdBi_2$ at $T = 0$ K (configurations No. 3 to No. 14) have an orthorhombic or a distorted orthorhombic lattice with space groups *Pnma* (#62), *Cmcm* (#63), *Cmce* (#64, the anti-La_2Sb type structure), *Cmmm* (#65), *Pnnm* (#58), and $I4_1$/a (#88) in addition to a tetragonal lattice with space group $I4_1$/amd (#141). For example, the USPEX24 configuration is a triclinic lattice with space group $P\bar{1}$ (#2) or an orthorhombic lattice with space group *Cmcm* (#63) by using a higher tolerance to determine the symmetry. Both configurations of No. 5 and No. 9 belong to the anti-La_2Sb type structure but with different number of atoms in the unit cell (24 atoms and 12 atoms, respectively; see **Table S1**).

[**Figure 7**]

The predicted XRD patterns of three $NdBi_2$ configurations are presented over $2\theta = 26–36°$ (F**igure S2**), in comparison with the measurement from the Nd-Bi alloy at $x_{\mathrm{Nd}} = 0.40$ with both the cubic NdBi and the $NdBi_2$ compounds (see **Figure 6**b). These XRD predictions are based on the Python library of pymatgen [43]. The additional peaks possibly from the $NdBi_2$ compound match reasonably well the anti-La_2Sb type configurations (No. 5 and No. 9) and the La_2Te type configuration (No. 19). We hence propose that $NdBi_2$ can be depicted by a mixture of the anti-La_2Sb configurations (with 12 and/or 24 atoms in the unit cell) as well as the La_2Te-type configurations (with 24 atoms). This approach agrees reasonably well with a distorted anti-La_2Sb configuration with 48 atoms in the unit cell ($P1$ or $P\bar{1}$), similar to the configuration of $LaBi_2$ and $NdBi_2$ suggested by Yoshihara et al. [14]. It is noted that the examination of the distorted anti-La_2Sb configuration with 48 atoms is beyond the scope of the present work.

The ΔH_0 values of the Nd-Bi compounds from the DFT predictions at $T = 0$ K are plotted in **Figure 7**b in comparison with experimental data at room temperature measured using an isoperibolic direct calorimeter by Borsese et al. [8] and using the Knudsen effusion method by

Viksman and Gordienko [9]. The predicted ΔH_0 values from the SCAN functional are much closer to the experimental data, especially for the compound of NdBi, than those from the PS and the PBE functionals. The average ΔH_0 difference between experiments and SCAN-predictions is about 6 kJ/mol-atom while the ΔH_0 value of cubic NdBi from SCAN (–111.26 kJ/mol-atom) is in excellent agreement with the measurements by a direct calorimetry (–111.4 ± 2.1 kJ/mol-atom[8]) and by the Knudsen effusion method (–116.25 kJ/mol-atom[9]), shown in **Table S4**. These results suggest that the selection of the X-C functional is essential to achieve accurate thermodynamic properties of the Nd-Bi compounds, as concluded previously [15]. The present CALPHAD-modeled ΔH_0 values agree with the modeled values by Wang et al. [5] ; however, both the modeling works predict more negative ΔH_0 values than the measurements by Borsese et al. [8] in the Nd-rich side. As indicated by Wang et al. [6], the modeled ΔH_0 values are acceptable by considering the agreements between most of the modeled and experimental values (including thermochemical and phase boundary data), as well as the large uncertainties from experiments; for example, the solubility of Nd in liquid Bi as shown in **Table 1** and **Figure 8**.

3.4 CALPHAD modeling of the Nd-Bi system

Thermodynamic modeling of the Nd-Bi system was performed using ESPEI [37] and PyCalphad [38] and the modeling parameters are summarized in **Table 2**. The calculated Nd-Bi phase diagram is illustrated in **Figure 8**, compared with the previous CALPHAD modeling by Wang et al.[6] and experimental data by Abulkhaev [7]. Only liquidus lines/data points from the previous modeling and measurements are shown for clarity. The present modeling of invariant reactions agrees well with the previously reported results [6,7,44] and includes a new peritectic reaction at 774 K with the Nd_3Bi_7 compound (**Table S5**). The present work calculated the eutectoid reaction of [(βNd of DHCP solution) ↔ (αNd of BCC solution) + Nd_2Bi] at 1124 K, slightly higher than the measured temperature at 1108 ± 10 K [7]. The liquidus at the Bi-rich side is higher than the previous results [6,7,44] as a result of incorporating new emf and the solubility data from this work and Smith [13]. The presently modeled ΔH_0 values at $T = 298$ K agree with the previous modeling work at $T = 298$ K by Wang et al.[6] and show a slight improvement in the Bi-rich side towards experimental data at room temperature by Borsese et al. [8] and Viksman and Gordienko [9] (**Figure 7**b).

[**Table 2**]

[**Figure 8**]

The activity of Nd in the Bi-rich liquid based on the present CALPHAD modeling is shown in **Figure 9**a (solid lines), compared to the emf measurements (symbols), and the previous modeling (dashed lines) by Wang et al.[6]. The presently modeled activity values agree well with the emf measurements, especially at low temperatures ($T = 773$ K and 873 K). The grey regions display the uncertainty quantification (UQ) of activity according to the EPSEI/PyCalphad modeling. The UQ ranges decrease with increasing temperature and the mean values of activity are much closer to the upper limit of the UQ range, especially at high temperatures. The enthalpy of mixing (ΔH_{mix}) of liquid at 973 K was also calculated from the present CALPHAD modeling and compared to the previous modeling work by Wang et al. [6] (**Figure 9**b). Note that the enthalpy of mixing of liquid is independent of temperature based on the present modeling as well as by Wang et al. [6]. The present ΔH_{mix} values are less negative than those from Wang et al. [6] by about 7 kJ/mol-atom at $x_{Nd} = 0.50$, making the presently modeled liquidus closer to the present measurements as well as those by Smith [13]. The uncertainty of ΔH_{mix} from the present ESPEI/PyCalphad modeling is small, i.e., ~ 0.3 kJ/mol-atom at $x_{Nd} = 0.50$.

[**Figure 9**]

4 Conclusions

The thermodynamic properties of the Nd-Bi alloys were investigated by combining both experimental and computational approaches. The emf data indicated a low activity of Nd in liquid Bi (e.g., $a_{\mathrm{Nd}} = 1.1 \times 10^{-13}$ at $T = 973$ K) implying strong chemical interactions between Nd and Bi. The solubility of Nd in liquid Bi was measured to be about 5.65 mol% at $T = 973$ K, lower than the previous value (9.55 mol%) by Abulkhaev [7]. A new peritectic transition reaction of [L + $NdBi_2$ = Nd_3Bi_7] was observed from thermal (DSC), structural (XRD), and microstructural (SEM-EDS) analyses. The configuration of $NdBi_2$ was suggested as a mixture of the anti-La_2Sb configuration and the La_2Te-type configuration using a data-mining approach in terms of structure-informed ML predictions of formation energy [15] for over 26,000 candidate $NdBi_2$ structures created by substituting species in AB_2-type configurations extracted from the literature and DFT databases through the MPDD database [20], followed by DFT-based verifications. The present CALPHAD modeling of the Nd-Bi system was conducted with the addition of new data using the high throughput ESPEI tool, including activity and solubility by emf measurements, phase transition temperatures by DSC, and the recently observed Nd_3Bi_7 compound, providing a more complete description of the Nd-Bi alloy system.

5 Acknowledgements

This work was supported by the U.S. Department of Energy (DOE) with Award No. DE-NE0008757 and the U.S. National Science Foundation (NSF) with Grant Nos. CBET-1844170 and CMMI-1825538. BJB acknowledges the supports from a NASA Space Technology Research

Fellowship (grant 90NSSC18K1168) and an NSF National Research Trainee Fellowship (grant DGE-1449785). First-principles calculations were performed partially on the Roar supercomputer at the Pennsylvania State University's Institute for Computational and Data Sciences (ICDS), partially on the resources of the National Energy Research Scientific Computing Center (NERSC) supported by the U.S. DOE under Contract No. DE-AC02-05CH11231, and partially on the resources of the Extreme Science and Engineering Discovery Environment (XSEDE) supported by NSF with Grant No. ACI-1548562.

6 References

[1] U.S Department of Energy, Critical Materials Strategy, 2012. https://www.energy.gov/sites/prod/files/DOE_CMS2011_FINAL_Full.pdf.

[2] J.L. Romero, S. a. McCord, Rare earth elements: procurement, application, and reclamation, 2012. http://prod.sandia.gov/techlib/access-control.cgi/2012/126316.pdf.

[3] G.B. Haxel, J.B. Hedrick, G.J. Orris, Rare Earth Elements-Critical Resources for High Technology, 2002. https://pubs.usgs.gov/fs/2002/fs087-02/.

[4] H. Kim, D.A. Boysen, J.M. Newhouse, B.L. Spatocco, B. Chung, P.J. Burke, D.J. Bradwell, K. Jiang, A.A. Tomaszowska, K. Wang, W. Wei, L.A. Ortiz, S.A. Barriga, S.M. Poizeau, D.R. Sadoway, Liquid metal batteries: Past, present, and future, Chem. Rev. 113 (2013) 2075–2099. https://doi.org/10.1021/cr300205k.

[5] T.P. Nigl, T. Lichtenstein, Y. Kong, H. Kim, Electrochemical Separation of Alkaline-Earth Elements from Molten Salts Using Liquid Metal Electrodes, ACS Sustain. Chem. Eng. 8 (2020) 14818–14824. https://doi.org/10.1021/acssuschemeng.0c04249.

[6] C.P. Wang, H.L. Zhang, A.T. Tang, F.S. Pan, X.J. Liu, Thermodynamic assessments of the Bi-Nd and Bi-Tm systems, J. Alloys Compd. 502 (2010) 43–48. https://doi.org/10.1016/j.jallcom.2010.03.042.

[7] V.D. Abulkhaev, Phase Diagram of the Neodymium-Bismuth System, Russ. J. Inorg. Chem. 46 (2001) 580–583.

[8] A. Borsese, R. Capelli, S. Delfino, R. Ferro, The heat of formation of neodymium-bismuth alloys, Thermochim. Acta. 8 (1974) 393–397. https://doi.org/10.1016/0040-6031(74)85107-5.

[9] G.S. Viksman, S.P. Gordienko, The thermodynamic characteristics of lanthanum,

praseodymium, neodymium, and gadolinium mono-bismuthides, Sov. Powder Metall. Met. Ceram. 26 (1987) 570–572. https://doi.org/10.1007/BF01156560.

[10] A. Ovchinnikov, J.P.A. Makongo, S. Bobev, Yet again, new compounds found in systems with known binary phase diagrams. Synthesis, crystal and electronic structure of Nd_3Bi_7 and Sm_3Bi_7, Chem. Commun. 54 (2018) 7089–7092. https://doi.org/10.1039/c8cc02563k.

[11] T. Yin, Y. Liu, D. Yang, Y. Yan, G. Wang, Z. Chai, W. Shi, Thermodynamics and Kinetics Properties of Lanthanides (La, Ce, Pr, Nd) on Liquid Bismuth Electrode in LiCl-KCl Molten Salt, J. Electrochem. Soc. 167 (2020) 122507. https://doi.org/10.1149/1945-7111/abb0f4.

[12] T. Lichtenstein, S. Im, C.T. Yu, H. Kim, Thermodynamic properties of rare-earth alloys by electrochemical emf measurements, J. Mater. Res. (2020) 1–9. https://doi.org/10.1557/jmr.2020.218.

[13] F.J. Smith, The solubilities of Thorium and Neodymium in liquid Lithium-Bismuth solutions, J. Less-Common Met. 27 (1972) 195–200.

[14] K. Yoshihara, J.B. Taylor, L.D. Calvert, J.G. Despault, Rare-earth bismuthides, J. Less-Common Met. 41 (1975) 329–337. https://doi.org/10.1016/0022-5088(75)90038-7.

[15] A.M. Krajewski, J.W. Siegel, J. Xu, Z.-K. Liu, Extensible Structure-Informed Prediction of Formation Energy with Improved Accuracy and Usability employing Neural Networks, ArXiv. (2020) arXiv:2008.13654.

[16] C.W. Glass, A.R. Oganov, N. Hansen, USPEX - Evolutionary crystal structure prediction, Comput. Phys. Commun. 175 (2006) 713–720. https://doi.org/10.1016/j.cpc.2006.07.020.

[17] A.O. Lyakhov, A.R. Oganov, H.T. Stokes, Q. Zhu, New developments in evolutionary structure prediction algorithm USPEX, Comput. Phys. Commun. 184 (2013) 1172–1182. https://doi.org/10.1016/j.cpc.2012.12.009.

[18] A. Novoselova, V. Smolenski, Electrochemical behavior of neodymium compounds in molten chlorides, Electrochim. Acta. 87 (2013) 657–662. https://doi.org/10.1016/j.electacta.2012.09.064.

[19] D. Shen, R. Akolkar, Electrodeposition of Neodymium from $NdCl_3$-Containing Eutectic LiCl–KCl Melts Investigated Using Voltammetry and Diffusion-Reaction Modeling, J. Electrochem. Soc. 164 (2017) H5292–H5298. https://doi.org/10.1149/2.0451708jes.

[20] A.M. Krajewski, J.W. Siegel, S.-L. Shang, Y. Wang, J. Xu, Z.-K. Liu, MPDD: The Material-Property-Descriptor Database, (2021).

[21] S. Kirklin, J.E. Saal, B. Meredig, A. Thompson, J.W. Doak, M. Aykol, S. Rühl, C. Wolverton, The Open Quantum Materials Database (OQMD): assessing the accuracy of DFT formation energies, Comput. Mater. 1 (2015) 15010. https://doi.org/10.1038/npjcompumats.2015.10.

[22] A. Jain, S.P. Ong, G. Hautier, W. Chen, W.D. Richards, S. Dacek, S. Cholia, D. Gunter, D. Skinner, G. Ceder, K.A. Persson, Commentary: The Materials Project: A materials genome approach to accelerating materials innovation, APL Mater. 1 (2013) 011002. https://doi.org/10.1063/1.4812323.

[23] K. Choudhary, K.F. Garrity, A.C.E. Reid, B. DeCost, A.J. Biacchi, A.R. Hight Walker, Z. Trautt, J. Hattrick-Simpers, A.G. Kusne, A. Centrone, A. Davydov, J. Jiang, R. Pachter, G. Cheon, E. Reed, A. Agrawal, X. Qian, V. Sharma, H. Zhuang, S. V. Kalinin, B.G. Sumpter, G. Pilania, P. Acar, S. Mandal, K. Haule, D. Vanderbilt, K. Rabe, F. Tavazza, The joint automated repository for various integrated simulations (JARVIS) for data-driven materials design, Npj Comput. Mater. 6 (2020) 173. https://doi.org/10.1038/s41524-020-00440-1.

[24] S. Gražulis, D. Chateigner, R.T. Downs, A.F.T. Yokochi, M. Quirós, L. Lutterotti, E.

Manakova, J. Butkus, P. Moeck, A. Le Bail, Crystallography Open Database – an open-access collection of crystal structures, J. Appl. Crystallogr. 42 (2009) 726–729. https://doi.org/10.1107/S0021889809016690.

[25] S. Gražulis, A. Daškevič, A. Merkys, D. Chateigner, L. Lutterotti, M. Quirós, N.R. Serebryanaya, P. Moeck, R.T. Downs, A. Le Bail, Crystallography Open Database (COD): an open-access collection of crystal structures and platform for world-wide collaboration, Nucleic Acids Res. 40 (2012) D420–D427. https://doi.org/10.1093/nar/gkr900.

[26] W. Zhang, A.R. Oganov, A.F. Goncharov, Q. Zhu, S.E. Boulfelfel, A.O. Lyakhov, E. Stavrou, M. Somayazulu, V.B. Prakapenka, Z. Konopkova, Unexpected Stable Stoichiometries of Sodium Chlorides, Science (80-.). 342 (2013) 1502–1505. https://doi.org/10.1126/science.1244989.

[27] A.R. Oganov, S. Ono, Theoretical and experimental evidence for a post-perovskite phase of $MgSiO_3$ in Earth’s D″ layer, Nature. 430 (2004) 445–448. https://doi.org/10.1038/nature02701.

[28] G. Kresse, J. Furthmüller, Efficient iterative schemes for ab initio total-energy calculations using a plane-wave basis set, Phys. Rev. B. 54 (1996) 11169–11186. https://doi.org/10.1103/PhysRevB.54.11169.

[29] G. Kresse, D. Joubert, From ultrasoft pseudopotentials to the projector augmented-wave method, Phys. Rev. B. 59 (1999) 1758–1775. https://doi.org/10.1103/PhysRevB.59.1758.

[30] J.P. Perdew, K. Burke, M. Ernzerhof, Generalized Gradient Approximation Made Simple, Phys. Rev. Lett. 77 (1996) 3865–3868. https://doi.org/10.1103/PhysRevLett.77.3865.

[31] J.P. Perdew, A. Ruzsinszky, G.I. Csonka, O.A. Vydrov, G.E. Scuseria, L.A. Constantin, X. Zhou, K. Burke, Restoring the Density-Gradient Expansion for Exchange in Solids and

Surfaces, Phys. Rev. Lett. 100 (2008) 136406. https://doi.org/10.1103/PhysRevLett.100.136406.

[32] J. Sun, A. Ruzsinszky, J. Perdew, Strongly Constrained and Appropriately Normed Semilocal Density Functional, Phys. Rev. Lett. 115 (2015) 1–6. https://doi.org/10.1103/PhysRevLett.115.036402.

[33] M. Methfessel, A.T. Paxton, High-precision sampling for Brillouin-zone integration in metals, Phys. Rev. B. 40 (1989) 3616–3621. https://doi.org/10.1103/PhysRevB.40.3616.

[34] P.E. Blöchl, O. Jepsen, O.K. Andersen, Improved tetrahedron method for Brillouin-zone integrations, Phys. Rev. B. 49 (1994) 16223–16233. https://doi.org/10.1103/PhysRevB.49.16223.

[35] S.-L. Shang, Y. Wang, D. Kim, Z.-K. Liu, First-principles thermodynamics from phonon and Debye model: Application to Ni and Ni_3Al, Comput. Mater. Sci. 47 (2010) 1040–1048. https://doi.org/10.1016/j.commatsci.2009.12.006.

[36] A.T. Dinsdale, SGTE data for pure elements, Calphad. 15 (1991) 317–425. https://doi.org/10.1016/0364-5916(91)90030-N.

[37] B. Bocklund, R. Otis, A. Egorov, A. Obaied, I. Roslyakova, Z.-K.K. Liu, ESPEI for efficient thermodynamic database development, modification, and uncertainty quantification: application to Cu–Mg, MRS Commun. 9 (2019) 618–627. https://doi.org/10.1557/mrc.2019.59.

[38] R. Otis, Z.-K. Liu, pycalphad: CALPHAD-based Computational Thermodynamics in Python, J. Open Res. Softw. 5 (2017) 1–11. https://doi.org/10.5334/jors.140.

[39] H.L. Lukas, S.G. Fries, B. Sundman, Computational Thermodynamics: The CALPHAD Method, Cambridge University Press, 2007.

[40] N. Saunders, A.P. Miodownik, CALPHAD (Calculation of Phase Diagrams): A Comprehensive Guide, Pergamon, Oxford; New York, 1998.

[41] N.H. Paulson, B.J. Bocklund, R.A. Otis, Z.-K. Liu, M. Stan, Quantified Uncertainty in Thermodynamic Modeling for Materials Design, Acta Mater. 174 (2019) 9–15. https://doi.org/10.1016/j.actamat.2019.05.017.

[42] M.E. Straumanis, The precision determination of lattice constants by the powder and rotating crystal methods and applications, J. Appl. Phys. 20 (1949) 726–734. https://doi.org/10.1063/1.1698520.

[43] S.P. Ong, W.D. Richards, A. Jain, G. Hautier, M. Kocher, S. Cholia, D. Gunter, V.L. Chevrier, K.A. Persson, G. Ceder, Python Materials Genomics (pymatgen): A robust, open-source python library for materials analysis, Comput. Mater. Sci. 68 (2013) 314–319. https://doi.org/10.1016/j.commatsci.2012.10.028.

[44] H. Okamoto, Neodymium-Mangnese and Neodymium-Tin phase diagram, J. Phase Equilibria. 15 (1994) 569–570.

TABLES

Table 1. Solubility of Nd (mol %) in liquid Bi at $T = 773-973$ K.

Temperature	This work	Smith [13]	Abulkhaev [7]
773 K	0.99	0.89	4.13
873 K	2.91	2.23	7.07
973 K	5.65	4.64	9.55

Table 2. The present thermodynamic models and modeling parameters for the Ni-Bi system in the international system of units (SI).

Phases	Models	Modeling parameters
Liquid (Liq)	$(\mathrm{Bi, Nd})_1$	${}^{0}L^{\mathrm{Liq}} = -210930 - 39.74T$
		${}^{1}L^{\mathrm{Liq}} = 3606 + 6.56T$
		${}^{2}L^{\mathrm{Liq}} = 97170 - 44.30T$
		${}^{3}L^{\mathrm{Liq}} = -8893$
BCC	$(\mathrm{Bi, Nd})_1$	${}^{0}L^{\mathrm{BCC}} = -150000$ [6]
		${}^{1}L^{\mathrm{BCC}} = 50000$ [6]
DHCP	$(\mathrm{Bi, Nd})_1$	$G_{\mathrm{Bi}}^{\mathrm{DHCP}} = {}^{0}G_{\mathrm{Bi}}^{\mathrm{Rho\_A7}} + 5000$ [6]
		${}^{0}L^{\mathrm{DHCP}} = 100000$ [6]
Rho_A7	$(\mathrm{Bi, Nd})_1$	$G_{\mathrm{Nd}}^{\mathrm{Rho\_A7}} = {}^{0}G_{\mathrm{Nd}}^{\mathrm{DHCP}} + 5000$ [6]
		${}^{0}L^{\mathrm{Rho\_A7}} = 50000$ [6]
$\mathrm{Nd_3Bi_7}$	$(\mathrm{Bi})_{0.7}(\mathrm{Nd})_{0.3}$	$G_{\mathrm{m}}^{\mathrm{Nd_3Bi_7}} = 0.7\ {}^{0}G_{\mathrm{Bi}}^{\mathrm{Rho\_A7}} + 0.3\ {}^{0}G_{\mathrm{Nd}}^{\mathrm{DHCP}} - 77900 + 10.28T$
$\mathrm{NdBi_2}$	$(\mathrm{Bi})_{0.667}(\mathrm{Nd})_{0.333}$	$G_{\mathrm{m}}^{\mathrm{NdBi_2}} = 0.667\ {}^{0}G_{\mathrm{Bi}}^{\mathrm{Rho\_A7}} + 0.333\ {}^{0}G_{\mathrm{Nd}}^{\mathrm{DHCP}} - 85340 + 10.63T$
NdBi	$(\mathrm{Bi})_{0.5}(\mathrm{Nd})_{0.5}$	$G_{\mathrm{m}}^{\mathrm{NdBi}} = 0.5\ {}^{0}G_{\mathrm{Bi}}^{\mathrm{Rho\_A7}} + 0.5\ {}^{0}G_{\mathrm{Nd}}^{\mathrm{DHCP}} - 113370 + 4.75T$
$\mathrm{Nd_4Bi_3}$	$(\mathrm{Bi})_{0.429}(\mathrm{Nd})_{0.571}$	$G_{\mathrm{m}}^{\mathrm{Nd_4Bi_3}} = 0.429\ {}^{0}G_{\mathrm{Bi}}^{\mathrm{Rho\_A7}} + 0.571\ {}^{0}G_{\mathrm{Nd}}^{\mathrm{DHCP}} - 113255 + 9.07T$
$\mathrm{Nd_5Bi_3}$	$(\mathrm{Bi})_{0.375}(\mathrm{Nd})_{0.625}$	$G_{\mathrm{m}}^{\mathrm{Nd_5Bi_3}} = 0.375\ {}^{0}G_{\mathrm{Bi}}^{\mathrm{Rho\_A7}} + 0.625\ {}^{0}G_{\mathrm{Nd}}^{\mathrm{DHCP}} - 113538 + 14.04T$
$\mathrm{Nd_2Bi}$	$(\mathrm{Bi})_{0.333}(\mathrm{Nd})_{0.667}$	$G_{\mathrm{m}}^{\mathrm{Nd_2Bi}} = 0.333\ {}^{0}G_{\mathrm{Bi}}^{\mathrm{Rho\_A7}} + 0.667\ {}^{0}G_{\mathrm{Nd}}^{\mathrm{DHCP}} - 106840 + 15.44T$

FIGURES

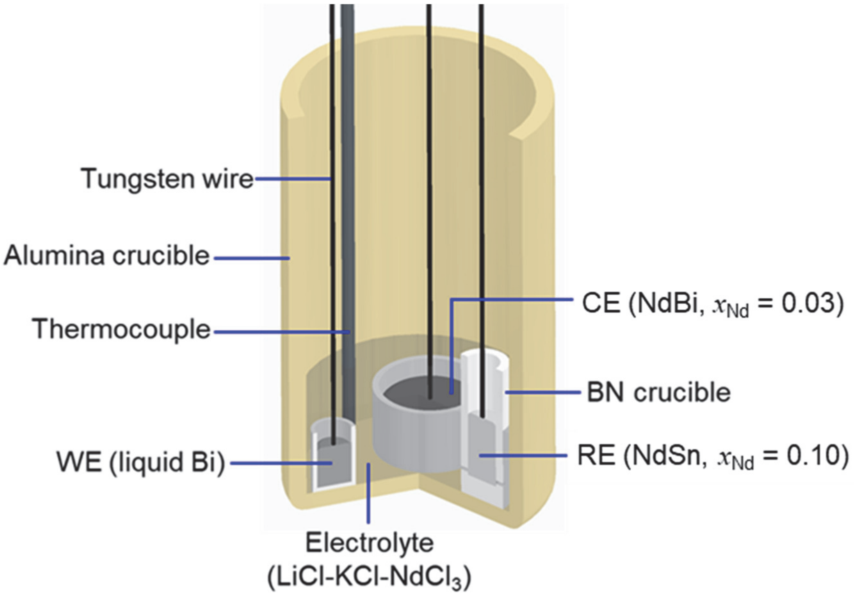

Figure 1. Three-electrode electrochemical cell configuration used for emf measurement of the Nd-Bi alloys via coulometric titration.

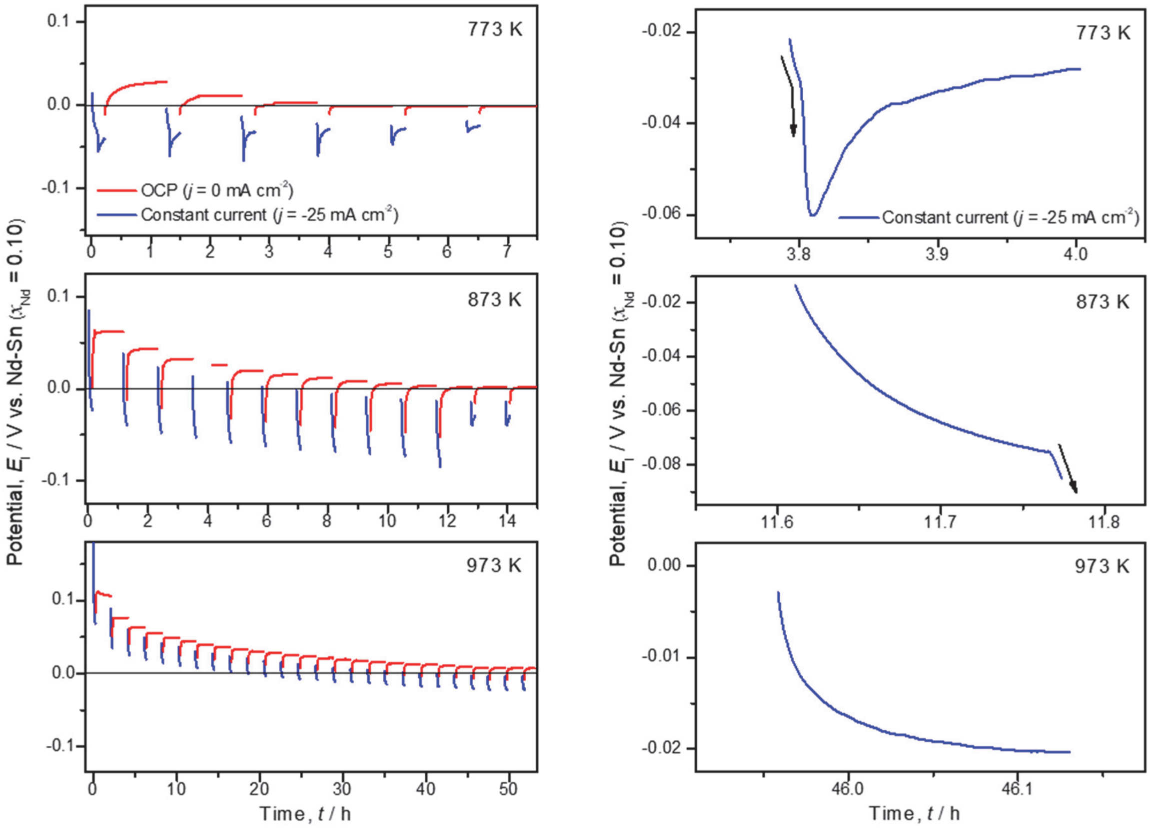

(a) (b)

Figure 2. (a) Continual coulometric titration Nd into liquid Bi WE: deposition of Nd at constant cathodic current density of 25 mA cm^{-2} followed by the OCP measurements at 773–973 K, (b) electrode potential during the deposition of Nd near the two-phase boundary at 773−973 K.

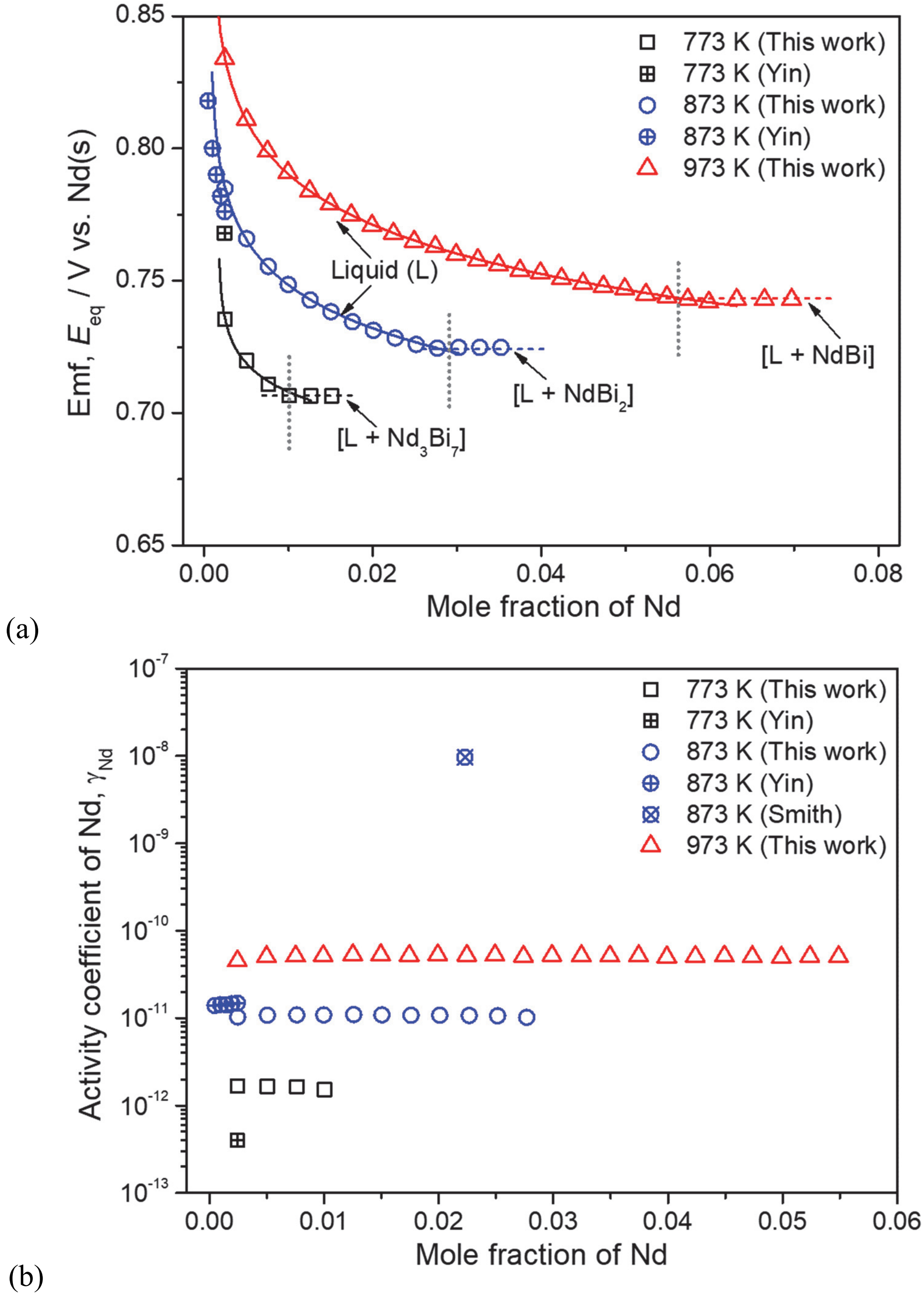

(a)

(b)

Figure 3. (a) Measured emf as a function of the mole fraction of Nd at 773–973 K, where solid lines represent logarithmic curve fit in the liquid phase and (b) activity coefficient of Nd (γ_{Nd}) in liquid, compared to the results by Yin et al.[11] and Smith [13].

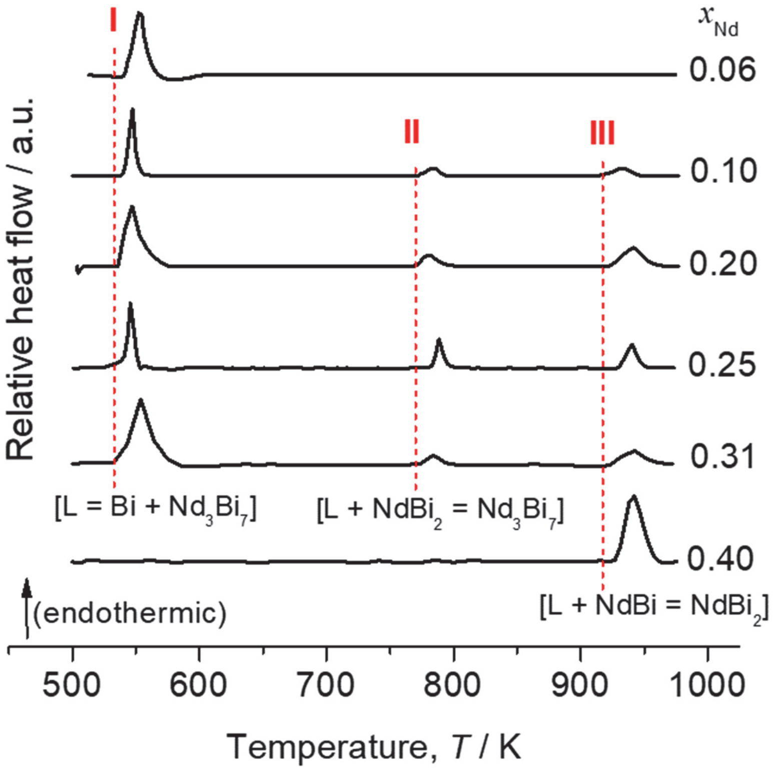

Figure 4. Representative DSC measurements of the Nd-Bi alloys (x_{Nd} = 0.06–0.40) during the heating cycle with 20 K min^{-1}, where the characteristic transitions are designated by the Roman numerals (I–III).

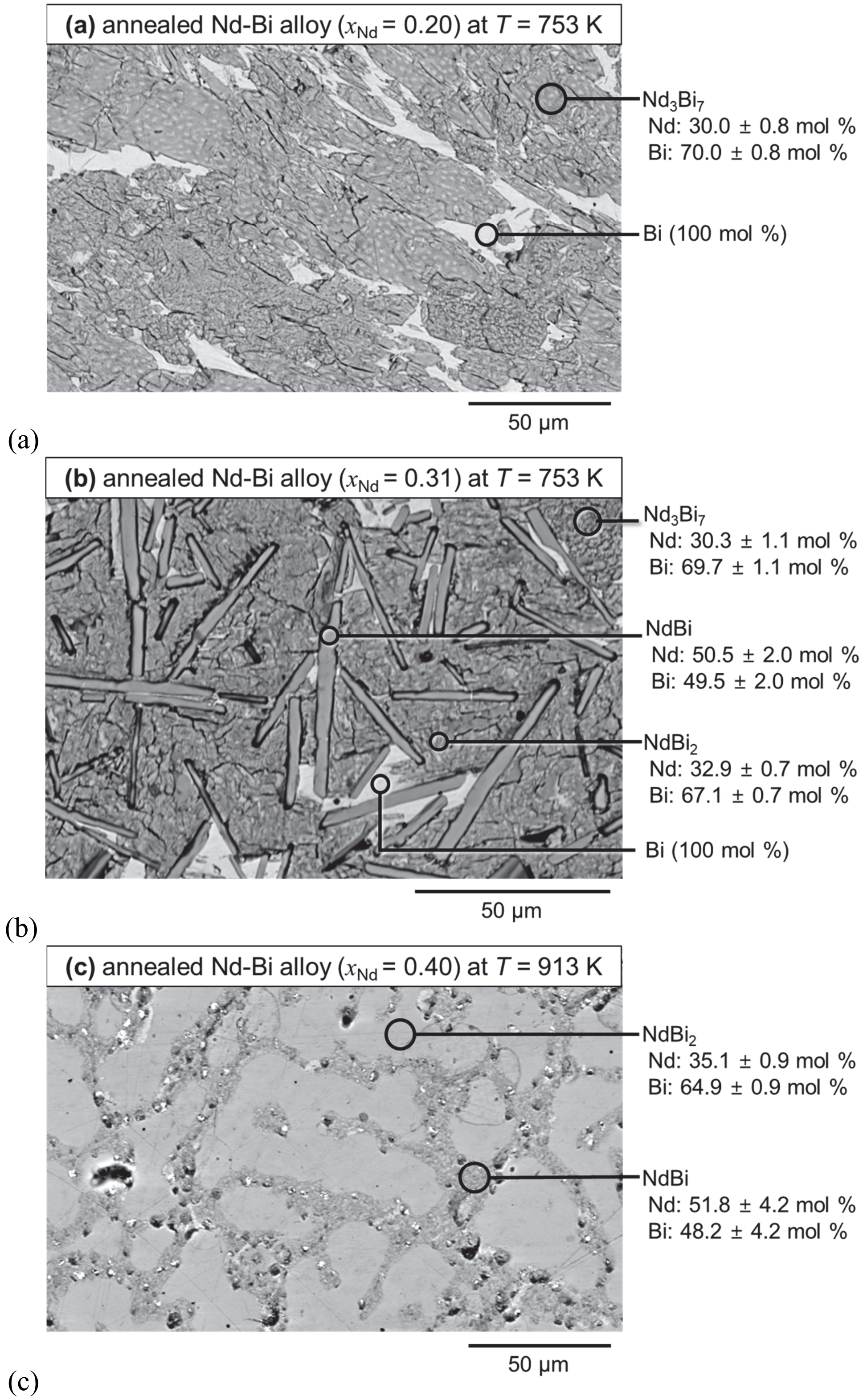

Figure 5. SEM images and EDS analyses for the annealed Ni-Bi alloys. (a) x_{Nd} = 0.20 annealed at T = 753 K, (b) x_{Nd} = 0.31 annealed at T = 753 K, and (c) x_{Nd} = 0.40 annealed at T = 913 K.

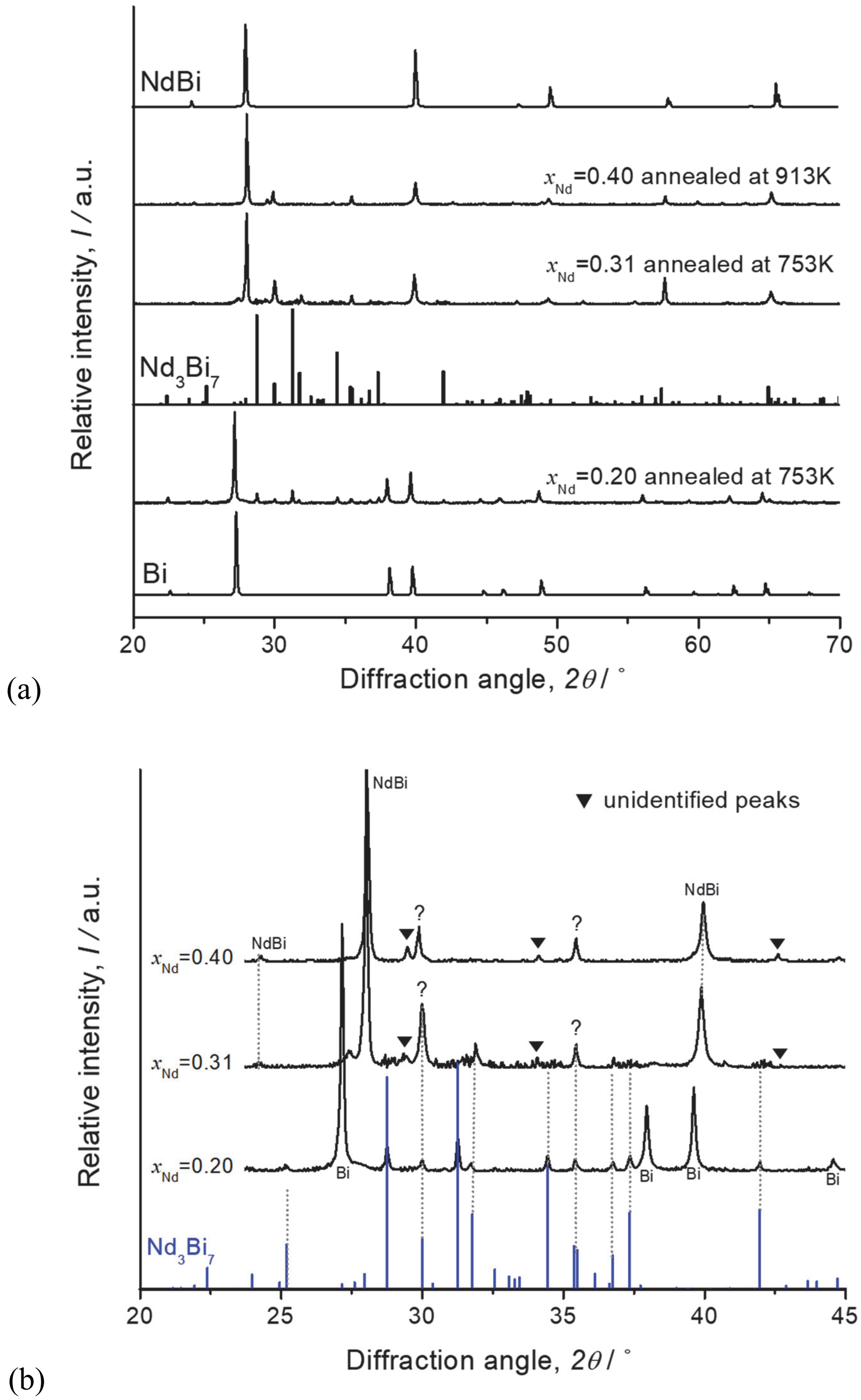

Figure 6. (a) XRD patterns of the annealed Nd-Bi alloys (x_{Nd} = 0.20, 0.31, 0.40) at 2θ = 20–70° and (b) enlarged view at 2θ = 20–45°, compared with the reported XRD patterns of the Bi, Nd_3Bi_7, and NdBi compounds[10,14,42].

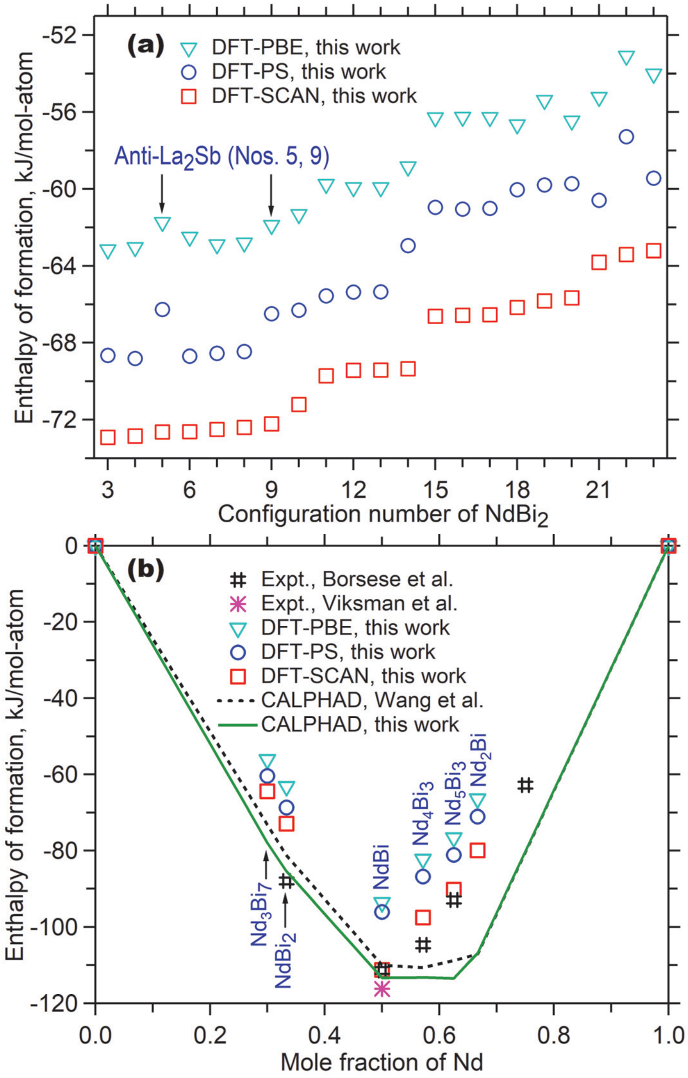

Figure 7. Enthalpy of formation (a) for the $NdBi_2$ configurations (No. 3 to No. 23) and (b) for the Nd-Bi compounds from the present first-principles predictions at 0 K (see more details in the Supplementary Excel file), in comparison with experimental data at room temperature by Borsese et al. [8], Viksman and Gordienko [9], and the CALPHAD modeled results at 298 K in the present work and by Wang et al.[6].

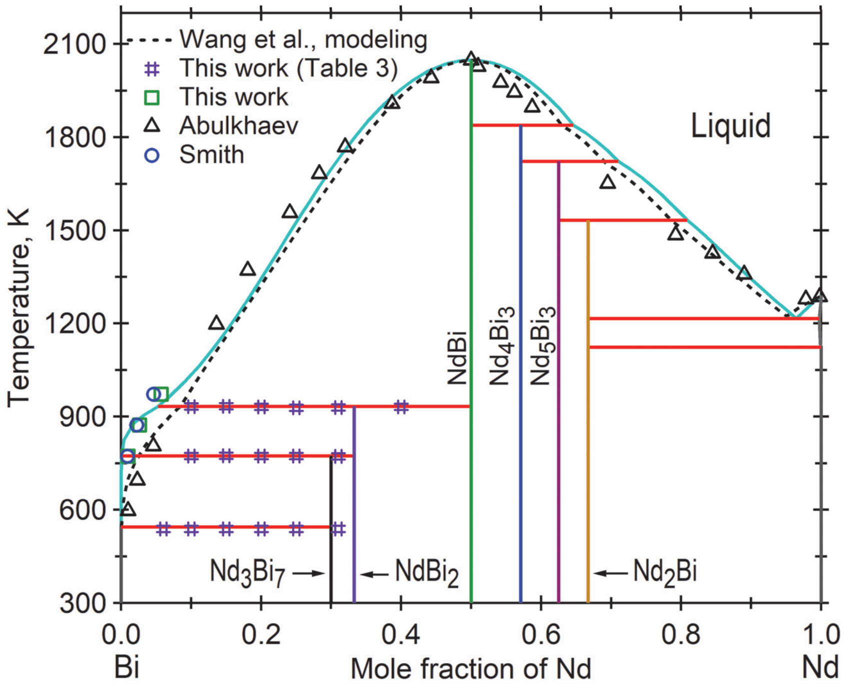

Figure 8. CALPHAD modeled Bi-Nd phase diagram in the present work (the solid lines) in comparison with the previous modeling by Wang et al. [6] (liquidus only, the dashed lines) and the measured phase boundaries (without invariant reactions for clarity) by Abulkhaev [7], Smith [13], and the present measurements (see data in **Table 1** and **Table S3**).

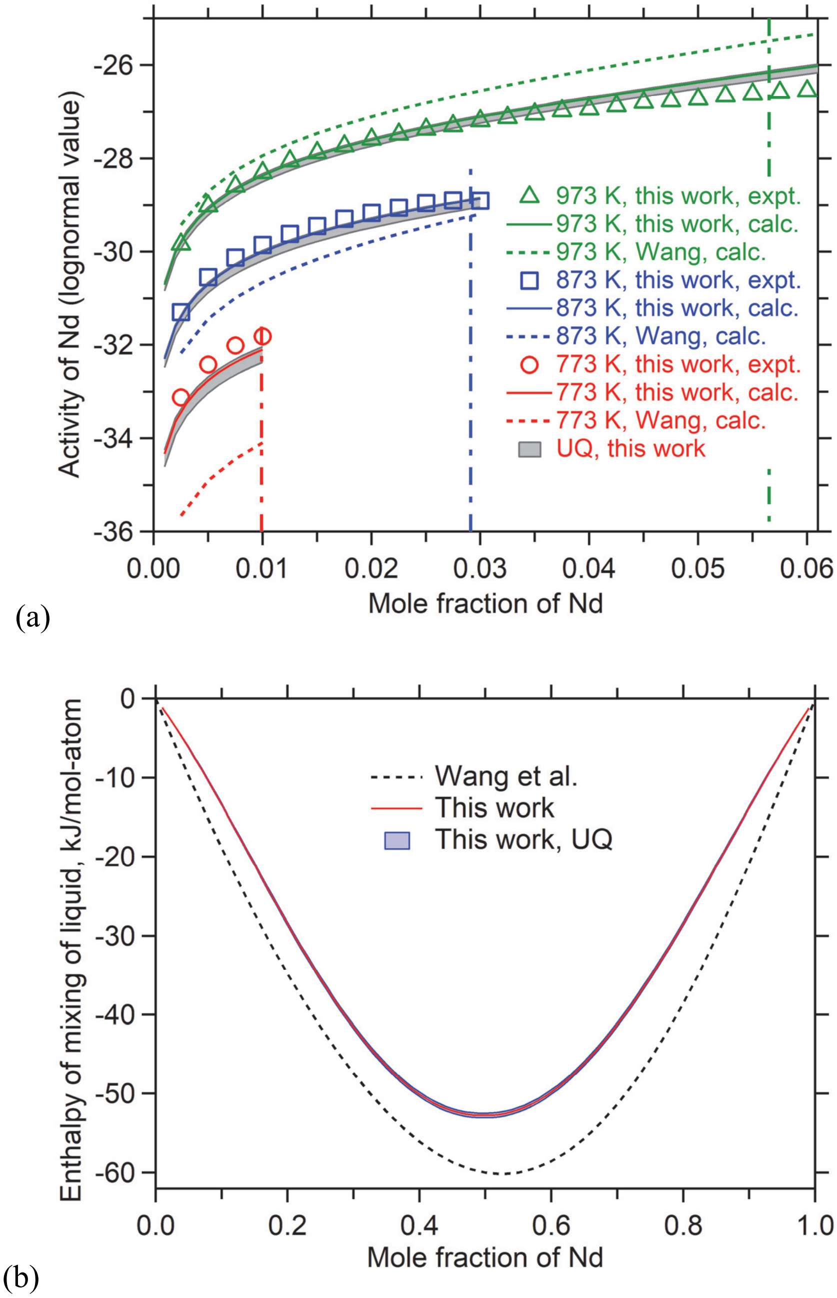

Figure 9. (a) The activity of Nd from CALPHAD modeling in the liquid phase only (the solid lines, where the composition of liquidus at each temperature is indicted by the vertical, dotted-dashed lines; see also **Table 1**) compared to experiments (symbols, from **Table S2**) with the stable DHCP phase of Nd as the reference state, and (b) enthalpy of mixing of liquid phase at 973 K. The grey and blue regions show uncertainty quantification (UQ) by the EPSEI/PyCalphad modeling, and the dashed lines are the previous CALPHAD modeling by Wang et al. [6].